



HAL
open science

Evaluation of scanning transmission X-ray microscopy at the Mn L_{2,3}-edges as a potential probe for manganese redox state in natural silicates

Franck Bourdelle, Emily Lloret, Cyril Durand, Laura Airaghi

► To cite this version:

Franck Bourdelle, Emily Lloret, Cyril Durand, Laura Airaghi. Evaluation of scanning transmission X-ray microscopy at the Mn L_{2,3}-edges as a potential probe for manganese redox state in natural silicates. *Physics and Chemistry of Minerals*, 2021, 48 (4), 10.1007/s00269-021-01142-w . insu-03192509

HAL Id: insu-03192509

<https://insu.hal.science/insu-03192509v1>

Submitted on 8 Apr 2021

HAL is a multi-disciplinary open access archive for the deposit and dissemination of scientific research documents, whether they are published or not. The documents may come from teaching and research institutions in France or abroad, or from public or private research centers.

L'archive ouverte pluridisciplinaire **HAL**, est destinée au dépôt et à la diffusion de documents scientifiques de niveau recherche, publiés ou non, émanant des établissements d'enseignement et de recherche français ou étrangers, des laboratoires publics ou privés.

1 Title: **Evaluation of scanning transmission X-ray microscopy at the Mn L_{2,3}-edges as a**
2 **potential probe for manganese redox state in natural silicates**

3
4 Authors: Franck Bourdelle^{a,*}, Emily Lloret^a, Cyril Durand^a, Laura Airaghi^b

5
6 Affiliations:

7 ^a Univ. Lille, Institut Mines-Télécom, Univ. Artois, Junia, ULR 4515 - LGCgE, Laboratoire
8 de Génie Civil et géo-Environnement, F-59000 Lille, France

9 ^b University of Orléans, CNRS, BRGM, ISTO, UMR 7327, F-45071, Orléans, France

10

11 *Corresponding authors:

12 Dr. Franck Bourdelle

13 Present mailing address: Laboratoire Génie Civil et géo-Environnement (LGCgE) –

14 Département des Sciences de la Terre, Université de Lille, Cité Scientifique, Bâtiment SN5,
15 59655 Villeneuve d'Ascq Cedex, France.

16 E-mail address: franck.bourdelle@univ-lille.fr

17 Phone number: + 33 (0)3 20 43 41 13

18

19 ORCID:

20 Franck Bourdelle: 0000-0002-7136-8692

21 Emily Lloret: 0000-0003-0952-9202

22 Cyril Durand: 0000-0001-8341-8450

23 Laura Airaghi: 0000-0001-7032-2732

24

25

26

27

28 **Abstract**

29 Determining the Mn valence variation at the nanometer scale will be an important advance in
30 the study of heterogeneous natural silicates. Here, the potential of the scanning transmission
31 X-ray microscopy at the Mn L_{2,3}-edges (640 - 655 eV) as a probe for manganese redox state is
32 evaluated. For this purpose, several natural Mn-silicates (rhodonite, ardennite, piemontite,
33 Mn⁴⁺-silicate, jacobsite), covering several Mn valence, were analysed to identify the spectral
34 parameters most sensitive to the Mn valence, regardless of the coordination environment, the
35 crystal field strength, the nature and the length of the metal–ligand bonds, and the intra-
36 atomic Coulomb and spin–orbit interactions. Two suitable spectral empirical calibrations are
37 thus proposed, linking the Mn valence to two peak intensity ratios: one ratio of intensities
38 from two energy points of the L₂ peak (at 651.7 and 655.2 eV), and one ratio of intensities
39 from one energy point of the L₂ peak (at 655.2 eV) and one of the L₃ peak (at 641.6 eV).
40 Thank to them, the first quantitative Mn valence maps are constructed, with a high spatial
41 resolution (< 40 nm pixel size), opening the way to exhaustive crystallochemical studies of
42 silicates containing Mn with different valences.

43

44 Key words: manganese valence; STXM; XANES spectroscopy; L_{2,3}-edges; redox mapping;
45 silicates

46

47 **Declarations**

48 Funding: This study was financially supported by LGCgE (laboratory funds).

49 Conflicts of interest/Competing interests: Not applicable.

50 Availability of data and material: XANES spectra are available on request from

51 franck.bourdelle@univ-lille.fr

52 Code availability: Not applicable.

53 Authors' contributions (optional): -

54 **1. Introduction**

55 Constraining redox conditions during sediment deposition, rock formation or
56 mineralogical transformation is of primary importance to understand the P-T-X history
57 (pressure-temperature-composition) of geological systems. Redox conditions are usually
58 assessed by the analysis of minerals since they partly influence their chemical composition.
59 The evaluation of redox conditions is often based on the iron redox state, i.e. by the
60 quantification of the $\text{Fe}^{3+}/\text{Fe}^{2+}$ ratio in minerals – mainly silicates, major constituents of crusts
61 – when they can contain both divalent and trivalent cations (i.e. Inoue et al. 2018). More
62 rarely, the redox state of other metals is investigated, as manganese. However, Mn – which
63 can be present as Mn^{2+} , Mn^{3+} and sometimes-but-rarely Mn^{4+} – could be a good indicator of
64 paleo-conditions of rock formation (Loomer et al. 2007), even if Mn-silicates, specially P-T-
65 X sensitive silicate solid solution such as phyllosilicates, are infrequent, at the very least not
66 ubiquitous in sedimentary and metamorphic rocks, and that the Mn content of these silicates
67 is low. In this way, Sussenberger et al. (2018) suggest that Mn content in chlorite could be a
68 proxy for chemo-stratigraphic conditions in depositional environment. For their part, Bobos et
69 al. (2018) establish a link between Mn-chlorite and Wolframite, the Mn content in chlorite
70 becoming an indicator of W-Mo mineralisation.

71 Unfortunately, authors could not determine the $\text{Mn}^{3+}/\text{Mn}^{2+}$ ratio which would have
72 noticeably modified the chlorite structural formula calculation, and potentially the subsequent
73 interpretations. In the past, different techniques have been envisaged for this purpose,
74 including electron microprobe analysis (EMPA, e.g. Albee and Chodos 1970), X-ray
75 photoelectron spectroscopy (XPS, e.g., Ilton et al. 2016) or X-ray absorption near edge
76 structure (XANES) spectroscopy at the K-edge (e.g. Manceau and Gallup 2005; Manceau et
77 al. 2012). However, none of these methods provides a nanometer-scale spatial resolution,
78 which could be particularly useful to identify chemical and redox zonation patterns in low-
79 temperature crystals (e.g. Bourdelle et al. 2018). On the other hand, several studies (e.g.,
80 Garvie and Craven 1994; van Aken and Liebscher 2002) have shown that electron energy-loss

81 spectroscopy (EELS) carried out in a transmission electron microscope (TEM) is a powerful
82 method for determining the redox state of transition metals at a submicrometric resolution,
83 including Mn in silicates, but sometimes induces severe beam damage effects, such as
84 electron beam-induced reduction of manganese (Lauterbach et al. 2000; de Groot et al. 2010;
85 Livi et al. 2012). The XANES spectroscopy at the $L_{2,3}$ -edges is often proposed as a powerful
86 alternative and is increasingly used in the Earth sciences. Firstly, the X-ray energies required
87 for XANES analysis are lower at the $L_{2,3}$ -edges (between ~640 and 655 eV) than at the K-
88 edge (between ~6500 and 6580 eV), allowing higher resolutions, i.e. < 0.1 eV and ~30 nm at
89 existing synchrotron facilities. Secondly, the X-ray incident beam is less destructive for
90 samples than the TEM-EELS electron beam.

91 The XANES spectroscopy at the $L_{2,3}$ -edges is based on the $2p \rightarrow 3d$ electronic
92 transition, which is sensitive to – among other parameters – the metal valence (e.g. Garvie and
93 Craven 1994). De Groot et al. (1994) describing in detail the complex physical basis of Mn
94 $L_{2,3}$ -edges, underlined that Mn valence can be obtained from $L_{2,3}$ -edge spectra by a multiplet
95 calculation. However, this approach remains difficult to use in the case of natural minerals
96 whose structure has not been beforehand determined. Otherwise, the Mn valence can be
97 evaluated by fitting $L_{2,3}$ -edge spectra with a combination of reference spectra, but this
98 requires Mn^{2+} , Mn^{3+} , Mn^{4+} reference compounds, with Mn in the same local coordination
99 environment than the studied sample. Consequently, several authors have turned to empirical
100 approaches, trying to find a spectral parameter depending only (or at least, mainly) on the Mn
101 valence. The white-line ratio, calibrated by van Aken and Liebscher (2002), is probably the
102 best known, linking the formal transition metal valence to the ratio of integral intensity (over
103 a 2 eV window) of the L_3 and L_2 excitation peaks. Recently, Wang et al. (2018) used the
104 integrated L-edge intensity, considering it is proportional to the total number of $3d$ holes
105 localized in the X-ray absorber (normalized to this invariant edge jump), while Risch et al.
106 (2017) proposed a linear correlation between Mn valence and the energy of the center of
107 gravity of the Mn L_3 -edge. But these methods, a review of which was proposed by Tan et al.

108 (2013), were often calibrated for Mn-oxides, but were not tested on Mn-silicates, which
109 present specific structures.

110 Moreover, synchrotron facilities make possible to carry out Mn L_{2,3}-edge XANES
111 spectroscopy with a scanning transmission X-ray microscope (STXM), one spectrum being
112 one image pixel of the studied sample area (e.g. Bourdelle et al. 2013). This makes it possible
113 to consider extracting quantitative maps of Mn valence over the entire area of interest, very
114 useful for heterogeneous natural samples containing mixed oxidation state Mn species. Pecher
115 et al. (2003) explore the feasibility of such maps extracted from STXM-XANES data, in order
116 to characterize the Mn charge state distribution in biominerals. Unfortunately, in absence of
117 empirical calibration based on a spectral intensity ratio rather than an integrated area or a
118 center of gravity calculation, the resulting maps remain qualitative.

119 From these observations, we want to evaluate the potential of the scanning
120 transmission X-ray microscopy at the Mn L_{2,3}-edges as a probe for manganese redox state
121 investigations in natural silicates, defining a suitable spectral empirical calibration allowing to
122 construct quantitative Mn valence maps with a high spatial resolution (nanoscale).

123

124 **2. Materials and methods**

125 2.1. Natural samples

126 Samples used in this study were natural silicates, containing various Mn amount and
127 covering the three common Mn redox state (2+, 3+, 4+). As the shape of the Mn L_{2,3}-edge
128 spectra can be influenced by, among others parameters, the Mn coordination, one oxide
129 presenting Mn in tetrahedral coordination sites is also considered. Particles transparent to soft
130 X-rays are needed to measure XANES spectra in the transmission mode of STXM, therefore
131 samples are prepared as grounded powders dispersing in ethanol; a drop of which is placed
132 (then evaporated) on a carbon holey support film placed on a 200 mesh copper grid.

133 The selected silicates are rhodonite, ardennite, piemontite and a Mn⁴⁺-silicate (Table
134 1), for which chemical composition has been verified by Energy-dispersive X-ray

135 spectroscopy, the EDX probe being coupled to a Scanning electron microscopy (QUANTA
136 200 SEM instrument operating at 15 kV with a 1.5 nA current; mineral standards used for
137 EDX probe calibration: albite, diopside, orthoclase, garnet and MnTiO₃; ZAF correction
138 applied). Rhodonite is a Mn²⁺ pyroxenoid, where Mn is mainly in 6 coordination, sometimes
139 in 7 (Smyth and Bish 1988; Nelson and Griffen 2005). Mn is therefore in distorted octahedral
140 sites, defined by Mn-O bonds. The rhodonite sample used here, whose formula is
141 Ca_{0.15}Mn_{0.85}SiO₃, comes from Gambaseta (Liguria, Italia). Ardennite is a Mn²⁺ sorosilicate
142 described by the following formula: Mn₄Al₄(AlMg)(AsO₄)(SiO₄)₂(Si₃O₁₀)(OH)₆. In it, Mn is
143 located in large polyhedron, based on 5 coordination via Mn-O bonds, and 2 additional
144 coordination via Mn-OH bonds (Donnay and Allmann 1968). Here, one specimen of As-
145 Ardennite from Salm-Château (Ardennes, Belgium) was studied; the composition does not
146 present an excess of Mn (< 4 atoms per formula unit), all Mn is consequently assumed as
147 Mn²⁺ (Nagashima and Armbruster 2020). Piemontite is a Mn-rich epidote, where Mn is in
148 trivalent form and occupies octahedral sites. The selected specimen comes from the Prabornaz
149 mine (Aosta, Italia), with the verified chemical formula
150 Ca_{2.05}(Al_{1.68}Fe³⁺_{0.49}Mn³⁺_{0.83})(Si_{2.0}O₇)(Si_{1.0}O₄)O(OH). The last studied Mn-silicate, a rare type
151 of silicates that contains tetravalent Mn similarly to stavelotite-(La), was sampled at
152 Eveslogchorr (Murmansk Oblast, Russia) combined with pectolite and has the determined
153 empirical formula: Na_{0.3}Ca_{1.4}Fe³⁺_{0.3}Mn⁴⁺₅SiO₁₄. A jacobsite sample, from Langban, (Filipstad,
154 Sweden), was also analysed. Jacobsite is an Mn²⁺ oxide belonging to the spinel group, with
155 the common formula MnFe₂O₄. As a “normal spinel”, Mn²⁺ occupies tetrahedral sites formed
156 by 4 oxygens (Bosi et al. 2019).

157

158 Table 1: Samples used for STXM-XANES Mn L_{2,3}-edge investigations to Mn mean valence
159 quantification

Type	Sample	Location	Mn valence	Position of major peaks (eV)	
				L ₃	L ₂
Silicate	Rhodonite	Gambaseta (Liguria, Italia)	2+	641.6	654.1

Silicate	Ardennite	Salm-Château (Ardennes, Belgium)	2+	641.6	654.1
Silicate	Piemontite	Prabornaz mine (Aosta, Italia)	3+	643.2	654.4
Silicate	Mn ⁴⁺ -silicate	Eveslogchorr (Murmansk Oblast, Russia)	4+	644.6	655.2
Oxide	Jacobsite	Langban (Filipstad, Sweden)	2+	641.6	654.1

160

161 2.2. STXM and XANES spectroscopy

162 The STXM is able to record the transmitted soft X-ray intensity on each point of the
163 pluri-micrometric-sized area of interest for each defined energy. Therefore, STXM gives 2D
164 images for which each pixel represents a soft X-ray absorption spectrum. This is of great
165 interest for mapping metal oxidation state variation into small crystallites (e.g. Bourdelle et al.
166 2013). In the present study, STXM analyses were acquired on the PolLux beamline at the
167 Swiss Light Source (SLS, Villigen, Switzerland). The characteristics of the beamline are
168 detailed by Raabe et al. (2008); the beam was in circular-polarisation configuration to avoid
169 crystal lattice orientation dependency of analysis (see below). The scanning transmission X-
170 ray microspectroscopy endstation allows to achieve stacks and linescans, i.e. a spectral map of
171 an area and a sum of spectra for each pixel of a line, respectively. Stacks were recorded over
172 the 635–660 eV energy range (Mn L_{2,3}-edge) using a 0.2 eV spectral resolution and a 40 nm
173 spatial resolution. Linescans were recorded over the same energy range, using a 0.1 eV
174 spectral resolution. The dwell time per image- and energy- point was between 1 and 10 ms.
175 Focus was checked systematically for each particle. STXM-XANES data were post-processed
176 using the aXis2000 software (Hitchcock 2012). Beam damages caused by the incident beam
177 were assessed by monitoring spectral changes at the Mn L_{2,3}-edges with increasing dwell
178 times up to 20 ms.

179

180 2.3. Spectrum processing

181 Spectra were extracted from stacks and linescans in form of optical density spectra
182 (noted OD), obtained as $OD = -\ln(I/I_0)$, where I is the X-ray intensity transmitted from the
183 sample, and I₀ is those recorded without samples. Then two steps of processing were applied
184 on spectra:

- 185 (i) a linear background correction was applied to remove the contribution of lower energy
 186 absorption edges, so that the pre-edge region is set to 0 optical density.
- 187 (ii) the two edge steps resulting from transitions to unoccupied states in the continuum were
 188 subtracted using a double arctan function (Chen et al. 1995; van Aken and Liebscher
 189 2002; Broton et al. 2007) as:

190

$$191 \quad f(\Delta E) = \frac{h_1}{\pi} \left(\tan^{-1} \left[\frac{\pi}{w_1} (\Delta E - E_1) \right] + \frac{\pi}{2} \right) + \frac{h_2}{\pi} \left(\tan^{-1} \left[\frac{\pi}{w_2} (\Delta E - E_2) \right] + \frac{\pi}{2} \right) \quad (1)$$

192

193 where h_1 and h_2 are the step heights of the two arctan functions, w_1 and w_2 are fixed peak
 194 widths and E_1 and E_2 are the positions of the inflection points resulting in an energy near the
 195 edge onset. Broton et al. (2007) proposed setting the function slope w at 5 eV, to account for
 196 the slow onset of the continuum. Following this recommendation, w_1 and w_2 were fixed to 5
 197 eV. For each sample, four or five spectra on different particles were extracted to evaluate the
 198 spectral variability. A total of 23 spectra were thus used in this study.

199

200 **3. Results and discussion**

201 3.1. Influences of Mn redox state, coordination and atomic environment on the shape of Mn 202 L_{2,3}-edge XANES spectrum

203 X-ray absorption near edge structure spectra at the Mn L_{2,3}-edges for Mn-silicates and
 204 jacobsite are shown in Figure 1, where peaks are identified by letters (from L₃-a to L₃-h and
 205 from L₂-a to L₂-e) and linear background is subtracted. These spectra result from transitions
 206 from 2*p* core electrons to 3*d* state, 4*s* state or continuum as follow:

- 207 - two strong absorption peaks, usually noted L₃ and L₂, due to the spin-orbit splitting of
- 208 2*p* level (van Aken and Liebscher 2002; Nishida et al. 2013) involving transitions
- 209 from 2*p*_{3/2} and 2*p*_{1/2} states to empty 3*d* atomic orbitals, respectively. From a 2*p*⁶3*d*^{*n*}
- 210 ground state, the absorption process leads to a core-excited 2*p*⁵3*d*^{*n*+1} final state, as 3*d*⁵
- 211 for Mn²⁺, 3*d*⁴ for Mn³⁺ and 3*d*³ for Mn⁴⁺, implying variations in absorption energy.

- 212 - edge jump steps at the bottom of L₃ and L₂ peaks, corresponding to 2*p* → continuum
213 transitions.
- 214 - negligible contributions of 2*p* → 4*s* transitions, which are 20 times weaker in intensity
215 than 2*p* → 3*d* transitions.

216 Each L₃ and L₂ peak consists of one major peak accompanied on both sides by several
217 minor peaks. The energy position of these major peaks mainly depends (but not only) on the
218 core-excited final state, i.e. Mn redox state: 641.6 and 654.1 eV for Mn²⁺ (L₃-b and L₂-c,
219 respectively; rhodonite, ardennite, jacobsonite), 643.2 and 654.4 eV for Mn³⁺ (L₃-e and L₂-d,
220 respectively; piemontite), 644.6 and 655.2 eV for Mn⁴⁺ (L₃-f and L₂-e, respectively; Mn⁴⁺-
221 silicate). In this way, spectra are qualitatively similar to those described in several previous
222 studies, obtained using different analytical techniques (e.g. Garvie and Craven 1994; Morales
223 et al. 2004; Zhang et al. 2010; Kubin et al. 2018).

224 Minor peaks arise from factors other than redox as their number, intensity and shape
225 vary from one sample to another. Therefore, Mn²⁺ spectra present 3 minor peaks (L₃-a, L₃-d
226 and L₃-g with a shoulder peak noted L₃-h) around L₃-b, and 2 minor peaks (L₂-a, L₂-b) before
227 L₂-c, more intensive (related to the intensity of major peaks) for rhodonite than for ardennite.
228 Mn³⁺ and Mn⁴⁺ spectra have fewer minor peaks: only two, at the same (or very close) energy
229 position than the L₃ and L₂ Mn²⁺ major peaks, and one more at 642.3 eV (L₃-c) only for Mn⁴⁺
230 spectra. These minor peaks are also observed in previous studies (e.g. de Groot et al. 2010;
231 Cuartero et al. 2016; Risch et al. 2017), especially on Mn-oxide spectra, and are influenced by
232 the Mn valence and coordination environment, the crystal field strength, the nature and the
233 length of the metal–ligand bonds, and the intra-atomic 3*d*-3*d* and 2*p*-3*d* Coulomb and spin–
234 orbit interactions in the 2*p* core and 3*d* orbitals.

235 Here, no complex calculations or multiplet analyses were used to describe spectrum shape in
236 detail as the aim of the present study is to propose an easy-to-use approach to empirically map
237 the Mn valence in silicates. However, some comments can be made to explain (i) the general
238 shape of the Mn-silicate spectra and (ii) the great similarity of them with Mn-oxide spectra.

239 In fact, $3d$ orbitals consist of five d orbitals, as three have lobes between x , y , z -axis
240 (noted d_{xy} , d_{xz} , d_{yz}) and two have lobes on the axes (noted d_{z^2} and $d_{x^2-y^2}$). In octahedral
241 coordination site, the 6 ligands approach Mn along the axes, increasing by electrostatic
242 repulsion the energy of d_{z^2} and $d_{x^2-y^2}$ orbitals (called e_g). Conversely, d_{xy} , d_{xz} , d_{yz} orbitals
243 (called t_{2g}) point between the ligands, that lowered their energies. This difference of energy
244 between e_g and t_{2g} orbital groups defines the crystal field strength (Δ_o or $10Dq$) (Burns 1993).
245 In the case of 6 coordinated Mn^{2+} , the t_{2g} spectral contribution is often assigned to the L_{3-a}
246 minor peak, while e_g is associated to the L_{3-b} major peak (Garvie and Craven 1994; de Groot
247 et al. 1994), $10Dq$ can be deducting from the energy distance between these two peaks. In the
248 Figure 2, focused on the L_{3-edge} part of Mn^{2+} absorption spectra (edge jump steps were
249 subtracted), the energy gap between L_{3-a} and L_{3-b} is very weak (< 1 eV), suggesting a low
250 $10Dq$ value. The comparison with $10Dq$ calculations and estimates from experiments
251 previously published (Garvie and Craven 1994; Garvie et al. 1994; Pérez-Dieste et al. 2004)
252 confirms that $10Dq$ value is probably around 0.5 or 1 eV. The energy difference between t_{2g}
253 and e_g orbital groups remains therefore weak enough for Mn to be in high-spin state (Burns
254 1993), which is the most common spin configuration for Mn (Garvie and Craven 1994; de
255 Groot 1994). The Figure 2 also shows that the energy position of L_{3-a} is always the same
256 whatever the Mn^{2+} mineral studied in our conditions, but that its intensity (related to L_{3-b}
257 major peak intensity) is variable. This observation is also suitable for other minor peaks L_{3-d}
258 and L_{3-g} , suggesting the contribution of another significant factors. In fact, Mn^{2+} in rhodonite,
259 ardenite and jacobsite is located in different coordination sites, with different Mn-ligand
260 bond length and different type of ligands. In rhodonite, Mn^{2+} occupies octahedral sites slightly
261 distorted, elongated, due to the global structure, linked to 6 O (Smyth and Bish 1988). This
262 configuration leads to an energy splitting between $d_{x^2-y^2}$ and d_{z^2} orbitals ($E_{d_{x^2-y^2}} > E_{d_{z^2}}$) on the
263 one hand, and between d_{xy} and d_{xz} , d_{yz} orbitals ($E_{d_{xy}} > E_{d_{xz}}$ and $E_{d_{yz}}$) on the other hand. In
264 ardenite, Mn^{2+} is located in large polyhedron with a 6 or 7 coordination configuration, with
265 O and OH as ligands (Donnay and Allmann 1968), also implying a substantial change in

266 orbital energies. In jacobsite, Mn^{2+} is surrounded by 4 O in a tetrahedral site. But in this case,
267 the 4 ligands are closer to the d_{xy} , d_{xz} , d_{yz} orbitals (t_2) than to the d_{z^2} , $d_{x^2-y^2}$ orbitals (e),
268 leading to an inversion of the splitting energy, t_2 orbital group having higher energy than e
269 orbital group (Burns 1993). Differences in spectrum shapes, especially the intensities of t_{2g} or
270 $t_g - L_3$ -a (virtually disappeared in the case of jacobsite), L_3 -d and L_3 -g peaks, must be related
271 to the coordination and the ligands of Mn. From an empirical point of view, the intensity of
272 minor peaks decreases proportionally to the number of Mn-O bonds. On the other hand, the
273 similarity of Mn-silicates (i.e. Mn^{2+} , Mn^{3+} and Mn^{4+} -silicates) and Mn-oxides spectra (from
274 this study and literature) tends to indicate that, as a first approximation, the extended atomic
275 environment (i.e. beyond the coordination site receiving Mn) has negligible influence
276 compared to that of the near coordination.

277 Consequently, an empirical calibration linking a spectral parameter to the Mn mean
278 valence must be mainly based on major peaks, most sensitive to redox, without taking into
279 account an energy window (as white line ratio method) that might include minor peaks, most
280 sensitive to the Mn coordination and the surrounding atomic environment. An empirical
281 calibration is possible especially since the $10Dq$ is weak (van der Laan and Kirkman 1992).

282

283 3.2. Mn redox state estimation from $L_{2,3}$ -edge XANES spectra

284 As three valence states of Mn could be present in silicates, it is not possible to
285 determine easily, directly and empirically the relative proportion of each of them. As an
286 alternative, XANES spectra allow to assess the Mn mean valence which, coupled to a
287 structural formula obtained with an independent method, gives a strong indication of the
288 likely $x\text{Mn}^{2+} + y\text{Mn}^{3+} + z\text{Mn}^{4+}$ combination.

289 As referenced in the Figure 1, the main variation in the XANES spectra of silicates
290 with the Mn valence involves the energy position of the L_3 major peak. More precisely, the L_3
291 major peak shifts to higher energies with increasing Mn charge, by a step of 1.4-1.6 eV.
292 However, because this step and Mn valence are not linearly linked, Risch et al. (2017) prefer

293 to use the center of gravity of the L₃-edge. From Mn-oxides, authors propose a linear
294 correlation implying to take in consideration the L₃ minor peaks in addition to major peaks. A
295 such correlation was established here for silicates (Figure 3), and demonstrates the influence
296 of minor peaks, i.e. of the type of coordination sites in which Mn occurs. Considering only the
297 mineral phases where Mn occupies octahedral sites (piemontite, rhodonite) and Mn⁴⁺-silicate,
298 the relationship between nominal Mn valence and the L₃ center of gravity is linear, with a R²
299 = 1. However, taking into account the ardennite in which Mn occupies large polyhedron or
300 jacobsite in which Mn is in tetrahedral sites, the energy position of the L₃ center of gravity for
301 Mn²⁺ phases depends on L₃-a, L₃-d and L₃-g peak weight and not only of Mn redox state.
302 Mainly, the L₃ center of gravity is a spectral parameter including a peak area, not extractable
303 from a stack. This approach therefore does not allow to easily map the Mn valence from
304 STXM-XANES data.

305 In order to construct a redox map, it becomes therefore necessary to propose a new
306 purely-empirical calibration of Mn valence with a simple spectral parameter, using selected
307 energy points (and not a spectral surface as white line ratio or center of gravity), that does not
308 need to have any physical significance (as an intensity ratio). Considering only the silicates
309 (jacobsite is excluded) and the 13 identified peaks (Figure 1), 78 ratios of two peak intensities
310 can be calculated, plus their inverses, namely 156 possibilities. But only 12 peak intensity
311 ratios are in correlation with the Mn valence with a coefficient of determination higher than
312 0.98. In fact, the R² is very poor for intensity ratios implying major peaks of Mn³⁺ and minor
313 peaks of Mn²⁺ (Figure 2). On the 12 peak intensity ratios correlated to Mn valence, 3 only
314 used peaks from L₃ peak, 6 only used peaks from L₂ peak, and 3 used peaks from L₃ and L₂
315 peaks. Among them, we prefer those using peaks common to several valences and major
316 peaks. Two correlations are therefore selected as calibration. The selected spectral parameter
317 in the first calibration is a ratio between the intensities at two energy points of the L₂-edge, i.e.
318 at L₂-a in Mn²⁺ spectra (651.7 eV) and at the L₂-e major peak in Mn⁴⁺ spectra (655.2 eV). The
319 spectral parameter is then expressed as follows:

320

$$321 \quad R_{L_2} = \frac{I(\text{at } 655.2 \text{ eV})}{I(\text{at } 651.7 \text{ eV})}$$

322

323 From this parameter, the first calibration equation is (Figure 4a):

324

$$325 \quad \text{Mn mean valence} = \frac{R_{L_2} + 6.705}{3.512} \quad (2)$$

326

327 It shows a coefficient of determination (R^2) of 0.999. The same R_{L_2} value is obtained for
328 ardenite and rhodonite (and jacobsite, not used for calibration), showing that R^2 is not
329 influenced by the Mn atomic environment but only by the Mn valence. This perfect
330 correlation can be used to map Mn valence on unknown samples, since only two images (at
331 fixed energy, i.e. 651.7 and 655.2 eV) are required.

332 The spectral parameter defined in the second calibration is the ratio between the
333 intensity at L₃-edge energy point (i.e. 641.6 eV, the energy position of the L₃-b major peak of
334 Mn²⁺ spectra) and the intensity at L₂-edge energy point (i.e. 655.2 eV, the energy position of
335 the L₂-e major peak of Mn⁴⁺ spectra). The calibration equation is expressed as follows (Figure
336 4b):

337

$$338 \quad \text{Mn mean valence} = \frac{R_{L_{2,3}} + 0.669}{0.386} \quad (3)$$

339 with

$$340 \quad R_{L_{2,3}} = \frac{I(\text{at } 655.2 \text{ eV})}{I(\text{at } 641.6 \text{ eV})}$$

341

342 The coefficient of determination for this second calibration (R^2) is 0.984, slightly lower than
343 the one of the first calibration. The difference between $R_{L_{2,3}}$ values for rhodonite and
344 ardenite (and jacobsite) suggests a contribution of Mn atomic environment in addition to the
345 Mn valence dependence. However, taking an intensity on the L₃-edge (which is more intense

346 than the L_2) and one on the L_2 -edge improves the signal to noise ratio. As for the first
347 correlation proposed, the construction of a Mn valence map from STXM-XANES data is
348 made possible by equation 3.

349

350 3.3. STXM-XANES coupling: Mn redox mapping

351 The scanning properties of the microscope allow to record a stack of 125 energy
352 images over the 635-660 eV with a spectral resolution of 0.2 eV. Equations 2 and 3 permit the
353 Mn mean valence to be estimated from the spectrum intensities at two energies. This gives the
354 possibility to easily map the Mn valence from two energy images, and use one of the two
355 calibrations proposed.

356 In fact, two other XANES images are required in addition to the two images used for
357 mapping, in order to subtract the background at each pixel of the images. Therefore, only four
358 energy images should be selected to calculate the R parameter. In the Figure 5, the calibration
359 procedure that uses the equation 3 and the $R_{L_2,3}$ parameter is drawn as example (piemontite
360 sample). It is obtained by extracting one image at 641.6 eV, one at 655.2 eV, one in the pre-
361 edge (to apply the “linear background correction” at each pixel of the 641.6 eV image), and
362 one beyond the energy corresponding to the L_2 peak (to remove the linear background and the
363 second edge step of the arctan function at each pixel of the 655.2 eV image). The ratio of
364 corrected 641.6 and 655.2 eV images can then be used to determine the $R_{L_2,3}$ for each pixel
365 and to obtain the map of Mn redox state. In this way, the linear background is represented by
366 only one energy at one energy position, so this point should be fairly close to the first peak
367 (638 eV in Figure 5). In the case of spectra with a strong background noise, it is possible to
368 make an “image average” (giving an average value of the linear pre-peak background) by
369 selecting about 10 images between 625 and 639 eV, by adding them and then by dividing the
370 resulting “image sum” by 10 thanks to the aXis2000 software.

371 If the equation 2 is chosen for calibration, the images required to calculate the R_{L_2}
372 parameter need to be selected at 651.7 eV (L_2 -a), at 655.6 eV (L_2 -e), at the inflexion point

373 between the L_3 peak and the L_2 peak (to remove the background from the 651.7 eV), and one
374 beyond the L_2 peak (to remove the linear background and the second edge step of the arctan
375 function for each pixel of the 655.2 eV image). By applying the same procedure as before, the
376 Mn map can be reconstructed only from the L_2 -edge data.

377 Resulting quantitative Mn redox maps are a useful tool to identify the Mn mean
378 valence of unknown nanometric particles, but have some limitations. On a map built from
379 $R_{L2,3}$ parameter for a no-pure piemontite sample constructed with equation 3 (Figure 6), the
380 Mn-free crystallites appear in white (Figure 5G and Figure 6) while in areas where the particle
381 is too thick and/or highly concentrated in Mn, valence is overestimated (Figure 6B). In the
382 first case, the absence of Mn leads to calculate the ratio between two too weak absorption
383 pixels (Figure 5E and F). In the second case, a too high X-ray absorption cause an absorption
384 saturation of the L_3 peak, which is more intense than the L_2 peak. This phenomenon generates
385 a nonlinear response of the absorption detection, artificially modifying the relative peak
386 intensities, affecting the $R_{L2,3}$ calculation and overestimating the Mn valence. Although more
387 sensitive to the signal/noise ratio, the use of the R_{L2} parameter and equation 2 to map the Mn
388 valence, based exclusively on the L_2 peak, may provide a favourable way to circumvent
389 absorption saturation issues encountered with the L_3 peak (Figure 6C).

390 The spatial averaging effect of the X-ray beam over the pixel size (i.e., 40 nm) must
391 also be taking into account. This effect fixes the limit of the minimum distance over which
392 phase contacts or phase rims can be discriminated.

393 Surpassing these limitations easily identifiable, the STXM-based XANES quantitative
394 map becomes a precise tool, giving an estimate of Mn valence with a high spatial resolution,
395 as demonstrated by the map of piemontite in the Figure 6.

396

397 3.4. Assessment of saturation and beam damage effects

398 Although EELS is known to cause more damage than STXM on the structure of
399 minerals (e.g. de Groot et al. 2010), the latter is nonetheless a method that damages particles

400 during analysis if precautions are not taken. Potentially, the repeated scan of particles at each
401 energy point of a spectrum can altered the structure of the crystallites, and consequently the
402 Mn mean valence estimate. A stack recorded on a 5x5 μm area, obtained with a spatial
403 resolution of 50 nm, a spectral resolution of 0.2 eV and a dwell time of 5 ms per energy- and
404 image- point results in a total analysis time of 2.5 hours (dead time excluded) and of 0.875 s
405 per image-point. To evaluate beam damages, spectral changes at the Mn $L_{2,3}$ -edges were
406 monitored with increasing dwell times, from 1 to 20 ms per energy- and image- point. The
407 resulting XANES spectra do not show significant changes, while R_{L2} and $R_{L2,3}$ parameters are
408 only slightly affected, varying by less than 5%. Consequently, the effect of beam damages on
409 the Mn valence estimate is negligible in the typical dwell time range used during routine
410 analyses.

411 The saturation of spectrum can also alter assessment of R_{L2} and $R_{L2,3}$ parameters (see
412 section 3.3). This phenomenon occurs when particles are too thick or too rich in Mn (or a
413 combination of both), leading to a distortion of the spectrum. Hanhan et al. (2009) for Ca and
414 Bourdelle et al. (2013) for Fe proposed to evaluate the maximum intensity of the major peak
415 not to be exceeded to avoid saturation effect. Applying a similar approach, the maximum Mn
416 L_3 peak intensity, below which the L_3/L_2 peak intensity ratio varies linearly and the spectrum
417 is undistorted, was determined. For this, a stack was recorded on a powder of piemontite
418 sample (Mn^{3+}) with particles of various thicknesses. Figure 7 plots the intensity of the L_3
419 major peak according to the one of L_2 major peak for each image-point. The intensities of
420 these two peaks increase linearly until ~ 0.25 OD. When the particle is thick enough for the L_3
421 major peak intensity to exceed 0.25 OD, the L_3/L_2 intensity ratio no longer evolves linearly,
422 i.e. the intensity of L_2 major peak increases faster than that of L_3 major peak, reflecting the
423 spectra distortion for the considered image-points. This observation is also valid for Mn^{2+} and
424 Mn^{4+} spectra. Consequently, all the quantitative data in this study were therefore obtained
425 from areas presenting a L_3 major peak intensity lower than 0.25 OD. It should be noted that
426 Mn is much more sensitive to saturation phenomena than Fe (saturation effects at > 1.5 OD at

427 the Fe L_{2,3}-edges; Bourdelle et al. 2013), i.e. saturation effects appear at relatively low Mn
428 content (concentration or weak sample thickness). On an indicative basis, piemontite, which
429 is a phase that is not very rich in Mn, presents saturated spectra for a crystallite thickness
430 higher than ~150 nm, while Mn-rich jacobsonite shows saturation effects on spectrum when
431 crystallite thickness is around 70 nm.

432 The crystal orientation compared with the direction of polarisation of the X-ray beam
433 may also influence the spectrum shape. This process is called linear dichroism (Benzerara et
434 al. 2011), and can be thwart using a circular polarized beam as here. The residual dichroism
435 effect was evaluated by comparing spectra from different piemontite particles with various
436 orientation. No change in spectrum shape was observed, and the impact of particle orientation
437 on the Mn mean valence estimate remained undetectable.

438

439 **5. Conclusion**

440 In the present work, we explore the possibility to construct quantitative Mn redox
441 maps for silicates using the STXM coupled with XANES spectroscopy at the Mn L_{2,3}-edges.
442 With fairly limited precautions, we demonstrate that this type of maps could be obtained from
443 two easy-to-use empirical calibrations linking the Mn mean valence to a simple ratio of
444 intensities from selected energy positions. We applied this approach on a mix of piemontite
445 and no-Mn phase sample, demonstrating the potential of it to assess the Mn valence at the
446 nanoscale through micrometric areas. Even if calibrations and map construction have yet to be
447 tested on silicates containing Mn under several oxidation states, as Mn-phyllsilicates, these
448 results pave the way for the study of nanochemical zonations in heterogeneous silicates.

449

450 **Acknowledgements**

451 We are most grateful to the PSI SLS synchrotron, especially Benjamin Watts (PolLux
452 beamline) for technical advice. Thanks are extended to Philippe Recourt (LOG, Univ. Lille)
453 for sample preparation and to Francis Coune for providing ardennite sample. The authors

454 wish also to thank the editor and the two anonymous reviewers for comments and suggestions
455 that improved the paper. This study was financially supported by LGCgE.

456

457 **References**

458 Albee AL, Chodos AA (1970) Semiquantitative electron microscope determination of
459 Fe^{2+}/Fe^{3+} and Mn^{2+}/Mn^{3+} in oxides and silicates and its application to petrologic
460 problems. *Am Mineral* 55:491-501.

461 Benzerara K, Menguy N, Obst M, Stolarski J, Mazur M, Tyliczak T, Brown GE Jr, Meibom
462 A (2011) Study of the crystallographic architecture of corals at the nanoscale by scanning
463 transmission X-ray microscopy and transmission electron microscopy. *Ultramicroscopy*
464 111:1268–1275

465 Bobos I, Noronha F, Mateus A (2018) Fe-, Fe,Mn- and Fe,Mg-chlorite: a genetic linkage to
466 W, (Cu, Mo) mineralization in the magmatic-hydrothermal system at Borralha, northern
467 Portugal. *Mineral Mag* 82:S259-S279

468 Bosi F, Biagioni C, Pasero M (2019) Nomenclature and classification of the spinel
469 supergroup. *Eur J Mineral* 31:183-192

470 Bourdelle F, Beyssac O, Parra T, Chopin C (2018) Nanoscale chemical zoning of chlorite and
471 implications for low-temperature thermometry: Application to the Glarus Alps
472 (Switzerland). *Lithos* 314:551-561

473 Bourdelle F, Benzerara K, Beyssac O, Cosmidis J, Neuville DR, Brown GE, Paineau E (2013)
474 Quantification of the ferric/ferrous iron ratio in silicates by scanning transmission X-ray
475 microscopy at the Fe L-2,L-3 edges. *Contrib Mineral Petrol* 166:423-434

476 Brotton SJ, Shapiro R, van der Laan G, Guo J, Glans PA, Ajello JM (2007) Valence state
477 fossils in Proterozoic stromatolites by L-edge X-ray absorption spectroscopy. *J Geophys*
478 *Res Biogeosci* 112:G3

479 Burns R (1993) Mineralogical Applications of Crystal Field Theory (Cambridge Topics in
480 Mineral Physics and Chemistry). Cambridge: Cambridge University Press.
481 doi:10.1017/CBO9780511524899

482 Chen CT, Idzerda YU, Lin HJ, Smith NV, Meigs G, Chaban E, Ho GH, Pellegrin E, Sette F
483 (1995) Experimental confirmation of the X-ray magnetic circular-dichroism sum-rules for
484 iron and cobalt. *Phys Rev Lett* 75:152–155

485 Cuartero V, Lafuerza S, Rovezzi M, Garcia J, Blasco J, Subias G, Jiménez E (2016) X-ray
486 absorption and emission spectroscopy study of Mn and Co valence and spin states in
487 $\text{TbMn}_{1-x}\text{Co}_x\text{O}_3$. *Phys rev B* 94:155117

488 de Groot FMF, de Smit E, van Schooneveld MM, Aramburo LR, Weckhuysen BM (2010) In-
489 situ scanning transmission X-ray microscopy of catalytic solids and related nanomaterials.
490 *Chem Phys Chem* 11:951–962

491 de Groot FMF (1994) X-ray absorption and dichroism of transition metals and their
492 compounds. *J Electron Spectros Relat Phenomena* 67:529-622

493 Donnay G, Allmann R (1968) Si_3O_{10} Groups in the Crystal Structure of Ardennite. *Acta*
494 *Cryst B* 24:845

495 Garvie LAJ, Craven AJ (1994) High-resolution parallel electron energy-loss spectroscopy of
496 Mn L_{2,3}-edges in inorganic manganese compounds. *Phys Chem Miner* 21:191-206

497 Garvie LAJ, Craven AJ, Brydson R (1994) Use of electron-energy loss near-edge fine
498 structure in the study of minerals. *Am Mineral* 79:411-425

499 Hanhan S, Smith AM, Obst M, Hitchcock AP (2009) Optimization of analysis of soft X-ray
500 spectromicroscopy at the Ca 2p edge. *J Electron Spectros* 173:44–49

501 Hitchcock AP (2012) aXis 2000 analysis of X-ray images and spectra. McMaster University,
502 Hamilton

503 Ilton ES, Post JE, Heaney PJ, Ling FT, Kerisit SN (2016) XPS determination of Mn oxidation
504 states in Mn (hydr)oxides. *Appl Surf Sci* 366:475–485

505 Inoue A, Inoue S, Utada M (2018) Application of chlorite thermometry to estimation of
506 formation temperature and redox conditions. *Clay Miner* 53:143–158

507 Kubin M, Guo M, Kroll T, Löchel H, Källman E, Baker ML, Mitzner R, Gul S, Kern J,
508 Föhlisch A, Erko A, Bergmann U, Yachandra V, Yano J, Lundberg M, Wernet P (2018)
509 Probing the oxidation state of transition metal complexes: a case study on how charge and
510 spin densities determine Mn L-edge X-ray absorption energies. *Chem Sci* 9:6813

511 Lauterbach S, McCammon CA, van Aken P, Langenhorst F, Seifert F (2000) Mossbauer and
512 ELNES spectroscopy of (Mg, Fe)(Si,Al)O₃ perovskite: a highly oxidised component of the
513 lower mantle. *Contrib Mineral Petrol* 138:17–26

514 Livi KJT, Lafferty B, Zhu M, Zhang S, Gaillot A-C, Sparks DL (2012) Electron Energy-Loss
515 Safe-Dose Limits for Manganese Valence Measurements in Environmentally Relevant
516 Manganese Oxides. *Environ Sci Technol* 46:970–976

517 Loomer D, Al T, Weaver L, Cogswell S (2007) Manganese valence imaging in Mn minerals
518 at the nanoscale using STEM-EELS. *Am Mineral* 92:72-79

519 Manceau A, Gallup DL (2005) Nanometer-sized divalent manganese-hydrous silicate
520 domains in geothermal brine precipitates. *Am Mineral* 90:371-381

521 Manceau A, Marcus MA, Grangeon S (2012) Determination of Mn valence states in mixed-
522 valent manganates by XANES spectroscopy. *Am Mineral* 97:816–827

523 Morales F, de Groot FMF, Glatzel P, Kleimenov E, Bluhm H, Hävecker M, Knop-Gericke A,
524 Weckhuysen BM (2004) In Situ X-ray Absorption of Co/Mn/TiO₂ Catalysts for Fischer-
525 Tropsch Synthesis. *J Phys Chem B* 108:16201-16207

526 Nagashima M, Armbruster T (2010) Ardennite, tiragalloite and medaite: structural control of
527 (As⁵⁺, V⁵⁺, Si⁴⁺)O₄ tetrahedra in silicates. *Mineral Mag* 74:55–71

528 Nelson WR, Griffen DT (2005) Crystal chemistry of Zn-rich rhodonite ("fowlerite"). *Am*
529 *Mineral* 90:969-983

530 Nishida S, Kobayashi S, Kumamoto A, Ikeno H, Mizoguchi T, Tanaka I, Ikuhara Y,
531 Yamamoto T (2013) Effect of local coordination of Mn on Mn-L2,3 edge electron energy
532 loss spectrum. *J Appl Phys* 114:054906

533 Pecher K, McCubbery D, Kneedler E, Rothe J, Bargar J, Meigs G, Cox L, Nealson K, Tonner
534 B (2003) Quantitative charge state analysis of manganese biominerals in aqueous
535 suspension using Scanning Transmission X-ray Microscopy (STXM). *Geochim*
536 *Cosmochim Acta* 67:1089–1098

537 Pérez-Dieste V, Crain J N, Kirakosian A, McChesney J L, Arenholz E, Young A T, Denlinger
538 J D, Ederer D L, Callcott T A, Lopez-Rivera S A, Himpsel FJ (2004) Unoccupied orbitals
539 of 3d transition metals in ZnS. *Phys Rev B* 70:085205

540 Raabe J, Tzvetkov G, Flechsig U, Böge M, Jaggi A, Sarafimov B, Vernooij MGC,
541 Huthwelker T, Ade H, Kilcoyne D, Tyliczszak T, Fink RH, Quitmann C (2008) PolLux: A
542 new facility for soft X-ray spectromicroscopy at the Swiss Light Source. *Rev Sci Instrum*
543 79

544 Risch M, Stoerzinger KA, Han B, Regier TZ, Peak D, Sayed SY, Wei C, Xu Z, Shao-Horn Y
545 (2017) Redox Processes of Manganese Oxide in Catalyzing Oxygen Evolution and
546 Reduction: An in Situ Soft X-ray Absorption Spectroscopy Study. *J Phys Chem C*
547 121:17682–17692

548 Smyth JR, Bish D L (1988) *Crystal Structures and Cation Sites of the Rock-Forming Minerals*
549 London and Boston (Unwin-Hyman Ltd.). *Mineral Mag* 52:733-734

550 Sussenberger A, Pospiech S, Schmidt ST (2018) [MnO vertical bar SiO₂, Al₂O₃, FeO, MgO]
551 balanced log-ratio in chlorites: a tool for chemo-stratigraphic mapping and proxy for the
552 depositional environment. 16th International Clay Conference (ICC) Location: Granada.
553 *Clay miner* 53:351-375

554 Tan H, Verbeeck J, Abakumov A, van Tendeloo G (2012) Oxidation state and chemical shift
555 investigation in transition metal oxides by EELS. *Ultramicroscopy* 116:24–33

556 van Aken PA, Liebscher B (2002) Quantification of ferrous/ferric ratios in minerals: new
557 evaluation schemes of Fe L-23 electron energy-loss near-edge spectra. *Phys Chem Miner*
558 29:188–200

559 Van der Laan G, Kirkman IW (1992) The 2p absorption spectra of 3d transition metal
560 compounds in tetrahedral and octahedral symmetry. *J Phys: Condens Matter* 4:4189-4204

561 Wang H, Friedrich S, Li L, Mao Z, Ge P, Balasubramanian M, Patil DS (2018) L-edge sum
562 rule analysis on 3d transition metal sites: from d10 to d0 and towards application to
563 extremely dilute metallo-enzymes. *Phys Chem Chem Phys* 20:8166–8176

564 Zhang S, Livi KJT, Gaillot A-C, Stone AT, Veblen DR (2010) Determination of manganese
565 valence states in (Mn³⁺, Mn⁴⁺) minerals by electron energy-loss spectroscopy. *Am*
566 *Mineral* 95:1741–1746

567

568 **Figure captions**

569

570 **Fig. 1** Representative XANES spectra at the Mn L_{2,3}-edges for the Mn-silicates and jacobsonite. The
571 spectra have been normalised to the major L₃ peak intensity, and some of the spectra have been shifted
572 vertically for clarity (normalised intensity with arbitrary units). The vertical lines indicate major peaks
573 (solid lines) and minor peaks (dashed lines). Each peak is indexed, redox states and core-excited final
574 state configurations are mentioned

575

576 **Fig. 2** Focus on L₃-edge for Mn²⁺ phases (rhodonite, ardenite, jacobsonite). The spectra have been
577 normalised to the major L₃ peak intensity. Coordination (number of O ligands and sites) is specified
578 for each phases

579

580 **Fig. 3** L₃-edge center of gravity from XANES spectra versus Mn valence for the selected silicates.
581 Error bars represent the standard deviation calculated on the base of 4 or 5 spectra for each sample.
582 Value for jacobsonite is given for information, but not taken into account for calibration calculation

583

584 **Fig. 4** $L_{2,3}$ -edge intensity ratio from XANES spectra versus Mn valence for the selected silicates. (A)
585 R_{L2} ratio, using selected intensities at two energy points (i.e. 651.7 and 655.2 eV) of the L_2 -edge. (B)
586 $R_{L2,3}$ ratio, using selected intensities at one energy point (i.e. 641.6 eV) of the L_3 -edge and one energy
587 point (i.e. 655.2 eV) of the L_2 -edge. Error bars represent the standard deviation calculated on the base
588 of 4 or 5 spectra for each sample, i.e. 18 spectra in total. Values for jacobsite are given for
589 information, but not taken into account for calibration calculation

590

591 **Fig. 5** Determination of the Mn valence from 4 selected energy images: one image in the pre-edge (to
592 apply the “linear background correction” at each pixel of the image; image A), one at 641.6 eV (L_3 -b
593 major peak of Mn^{2+} ; image B), one at 655.2 eV (L_2 -e major peak of Mn^{4+} ; image C) and one beyond
594 the L_2 -edge (to remove the edge step of the arctan function; image D). Finally, the ratio of the
595 resulting 641.6 and 655.2 eV images (E and F) can be used to determine the $R_{L2,3}$ parameter at each
596 pixel of the image and obtain Mn redox mapping (G). All images are OD images, where piemontite
597 and no Mn-silicate are the light-grey and dark phases on image E, respectively. White scale: 1 μm

598

599 **Fig. 6** Quantitative Mn redox nanomapping on particles from no-pure piemontite sample. A: optical
600 density image at 641.6 eV, where the piemontite and no-Mn silicate particles are the light-grey and
601 white phases, respectively. B: manganese redox mapping, calculated from the $R_{L2,3}$ parameter coupled
602 with the Eq. (3). C: manganese redox mapping, calculated from the R_{L2} parameter coupled with the Eq.
603 (2). The spatial averaging effect of the X-ray beam over the pixel size (i.e., 40 nm) sets the limit of the
604 minimum distance (turquoise rims, underlined by a yellow square). No-Mn silicates, identified by blue
605 dashed polygon on the OD image, appear in white on the redox map B and in black for no Mn
606 absorption on the redox map C and image E of the Fig. 5. Areas where the particle thickness is too
607 high to obtain no-saturated images (see section 3.4.) – highlighted by a purple polygon on the OD
608 image – lead to the overestimate of Mn valence (pink and red zones of the redox map B), up to the
609 total saturation (appearing in white on the map). Areas presenting no-too-thick piemontite particles
610 (i.e. the rest of the OD image) appear in blue on the Mn redox maps, testifying of trivalent manganese

611

612 **Fig. 7** Difference, pixel by pixel, of intensity detected between the L₃ major peak and the L₂ major
613 peak images (in which a pre-edge image was subtracted) for a no-pure piemontite sample (4661
614 pixels). The dashed line was calculated from a quadratic equation. Insets: representative spectra and
615 optical density image (641.6 eV) for a no-pure piemontite sample

Figure 1

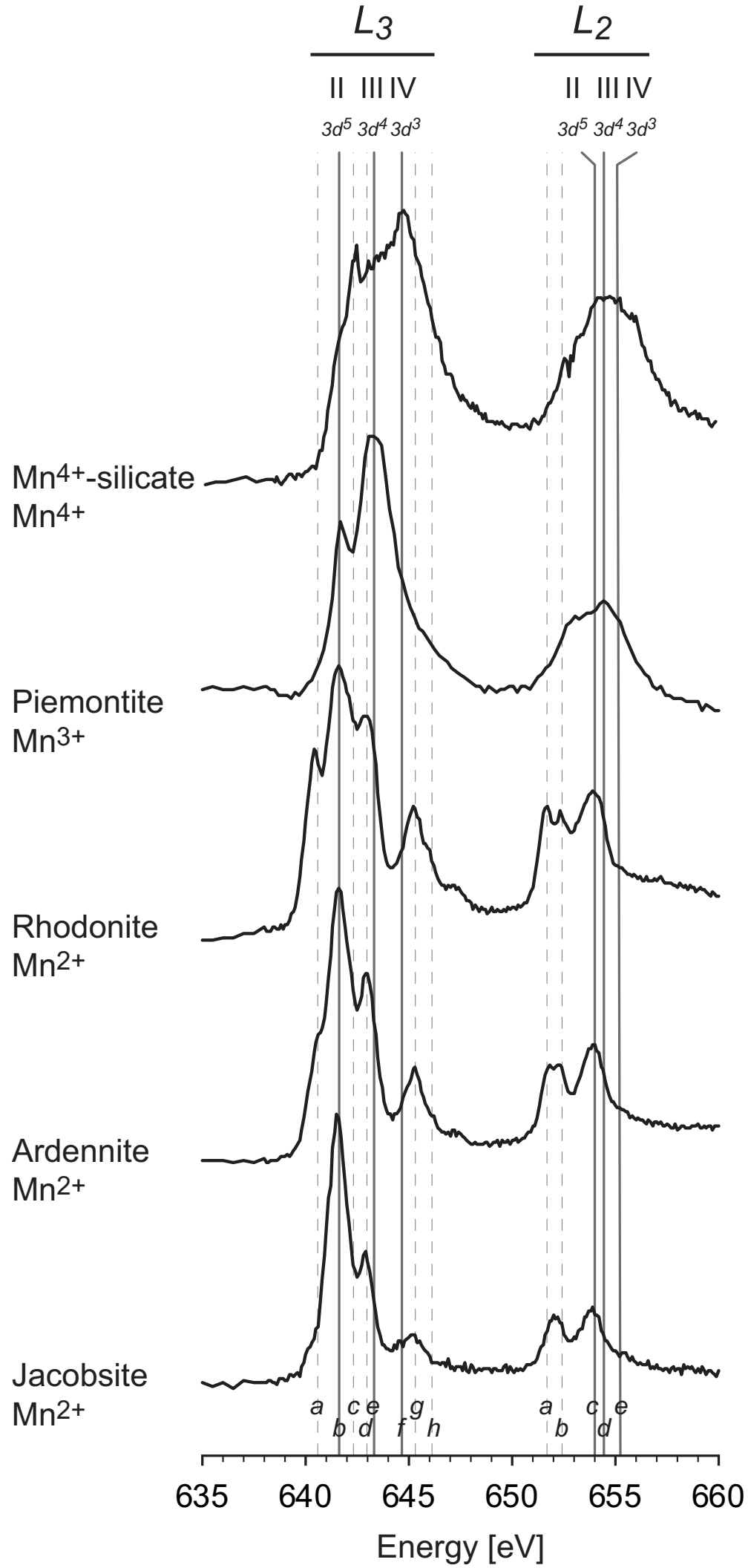


Figure 2

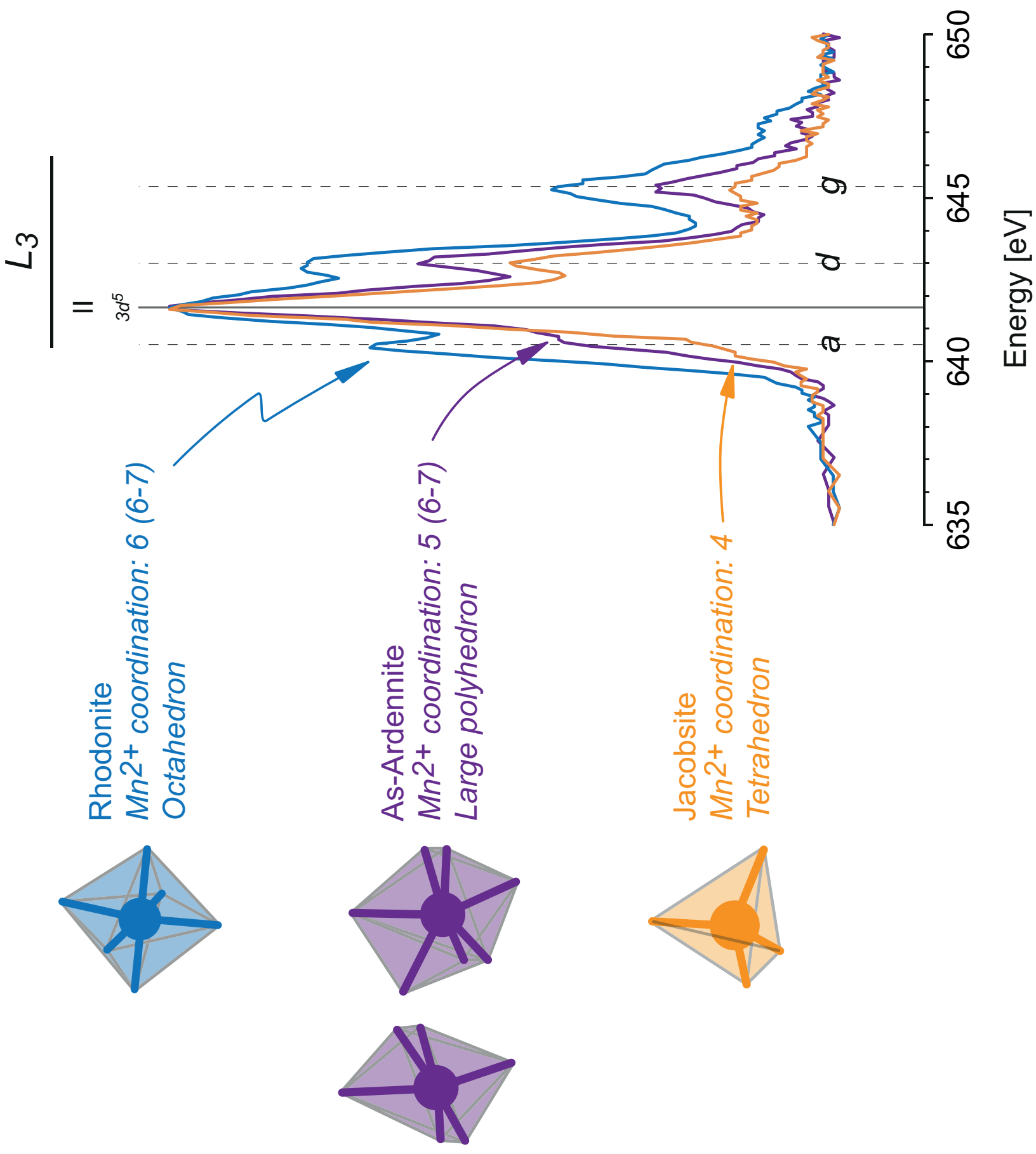


Figure3

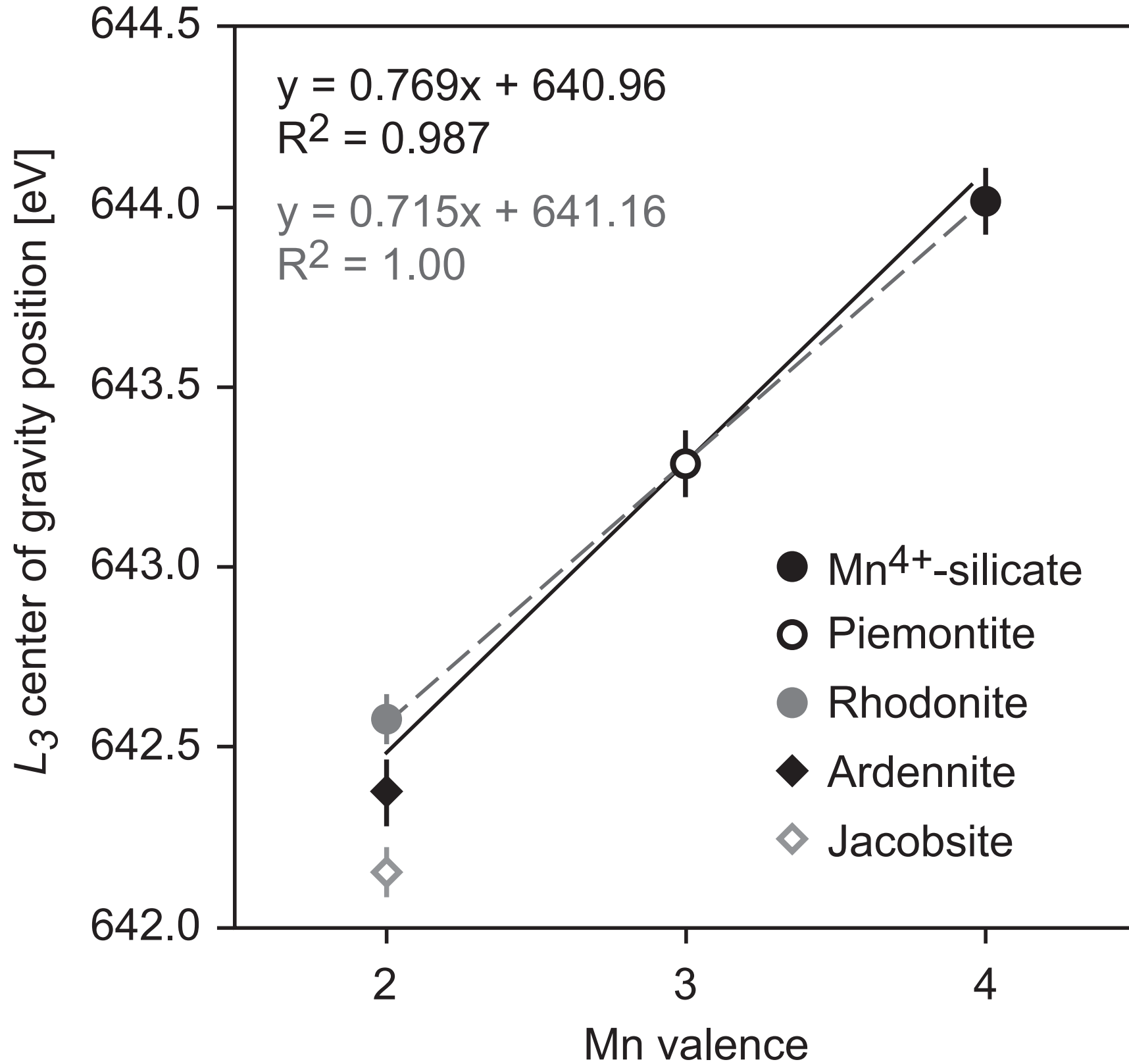
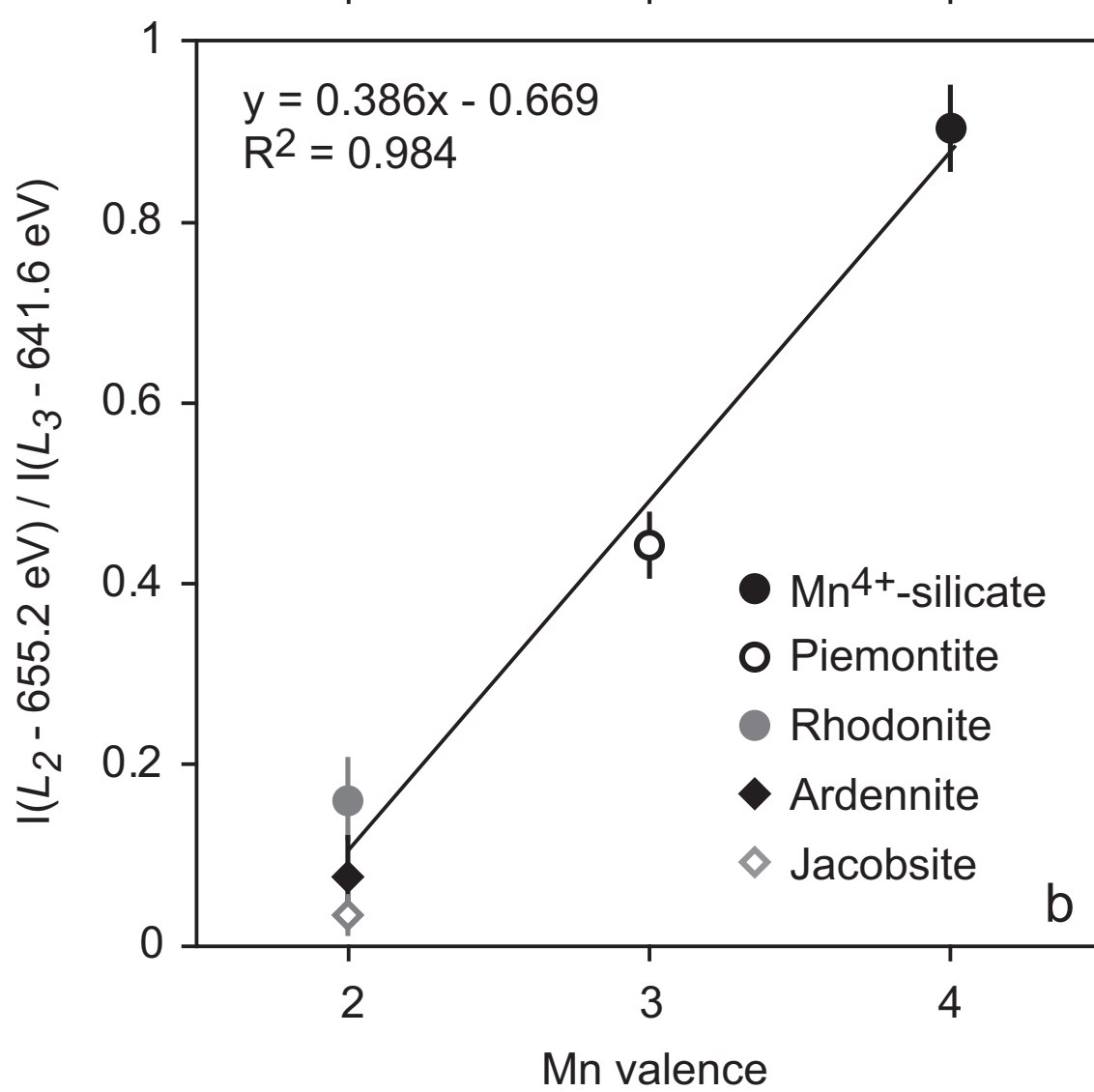
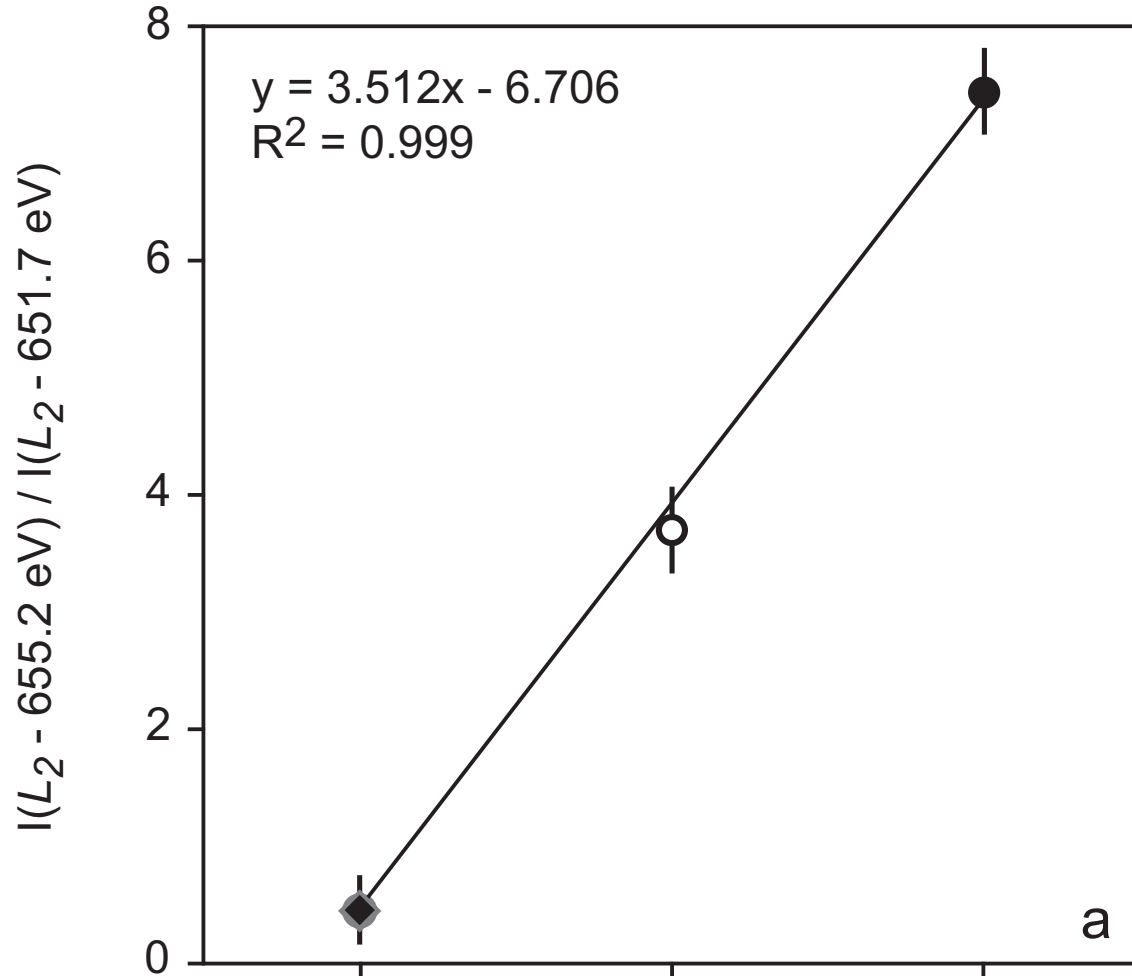
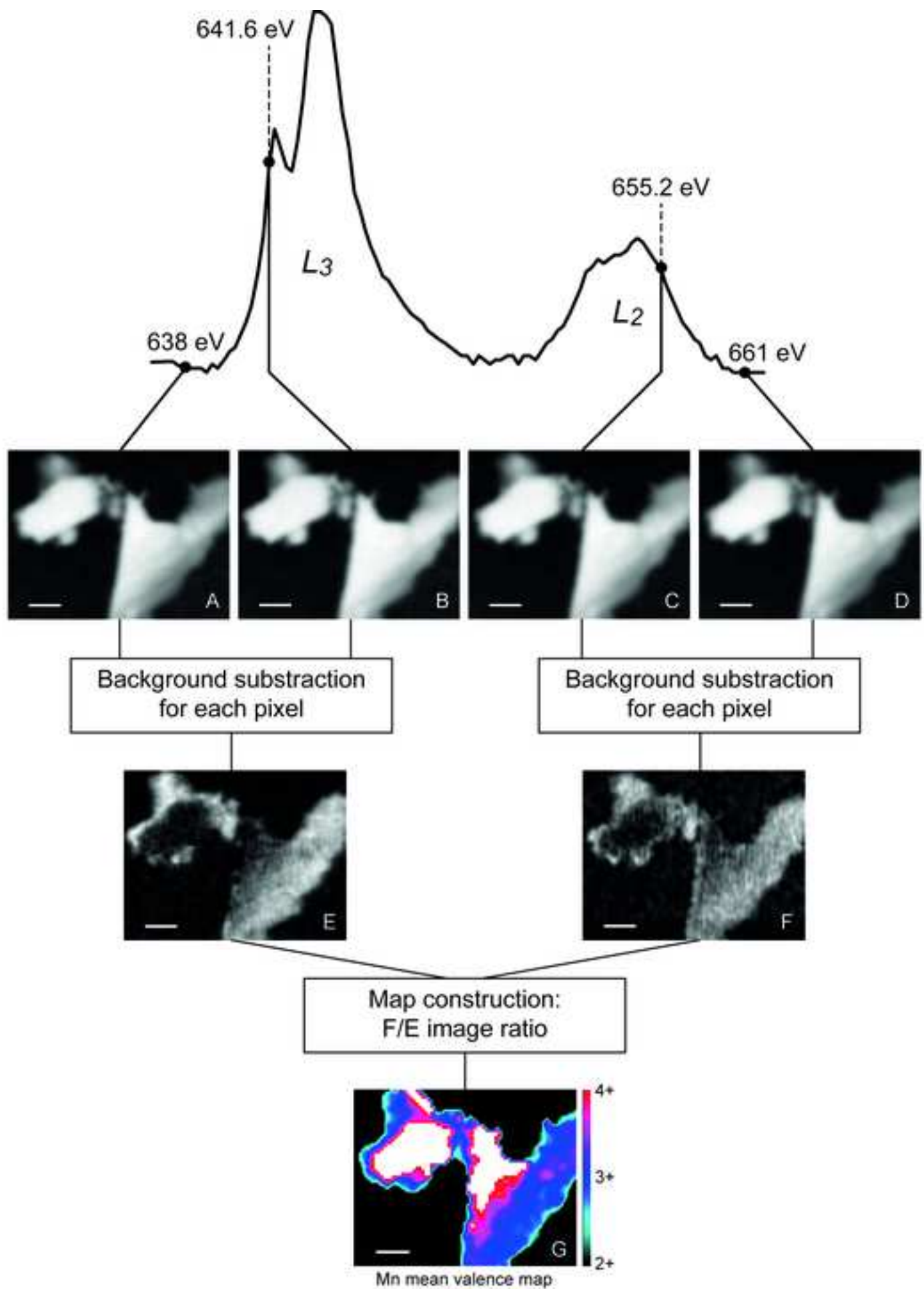


Figure 4





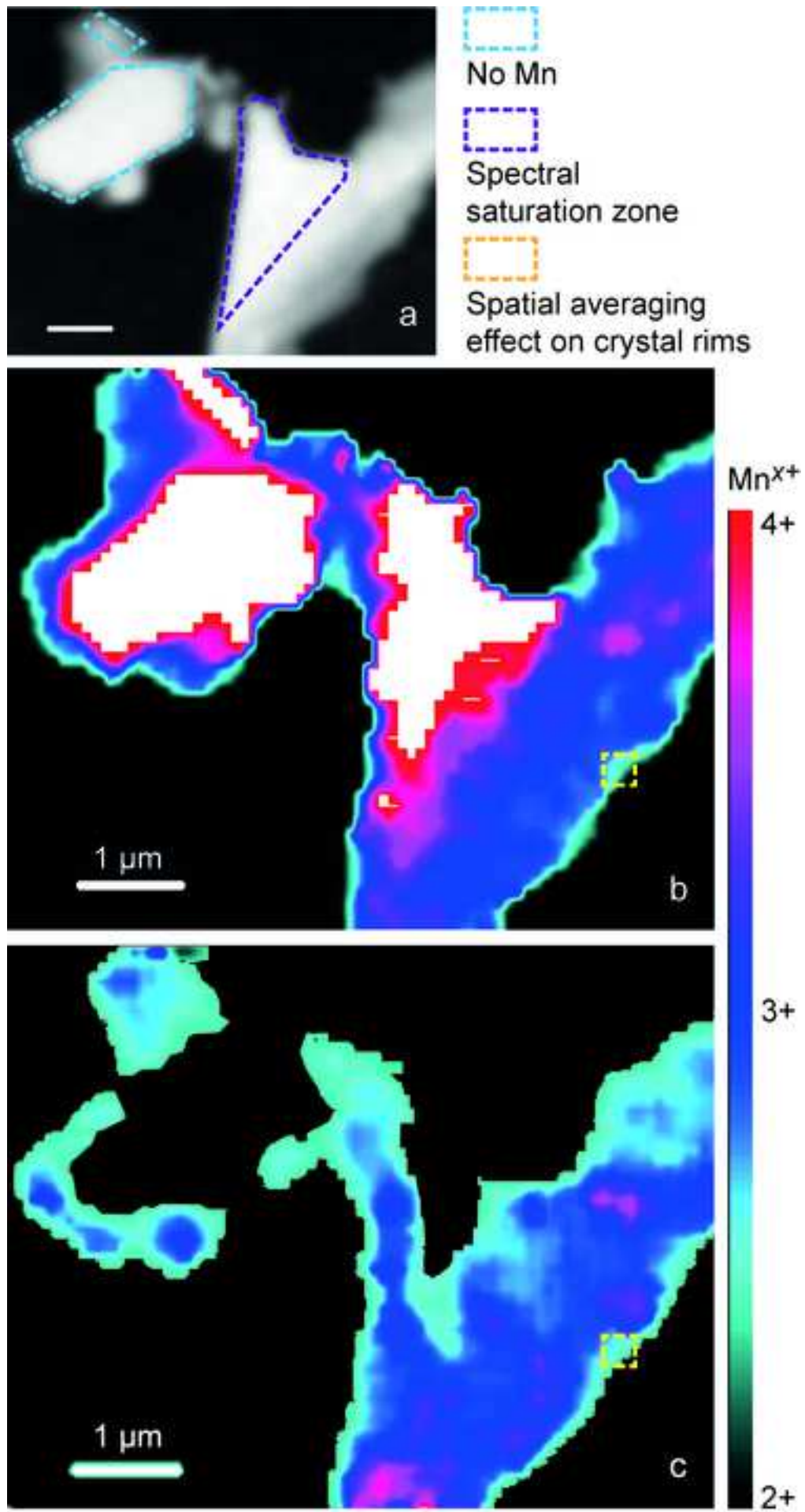


Figure 7

